

Ground-to-Air Gas Emission Rate Inferred from Measured Concentration Rise within a Disturbed Atmospheric Surface Layer

J. D. WILSON AND T. K. FLESCH

Department of Earth and Atmospheric Sciences, University of Alberta, Edmonton, Alberta, Canada

P. BOURDIN

Flight Sciences Group, Bombardier Aerospace, Toronto, Ontario, Canada

(Manuscript received 28 October 2009, in final form 21 April 2010)

ABSTRACT

In reference to previously observed concentrations of methane released from a source enclosed by a windbreak, this paper examines a refined “inverse dispersion” approach for estimating the rate of emission Q from a small ground-level source, when the surface-layer winds near that source are highly disturbed. The inverse dispersion method under investigation is based on simulation of turbulent trajectories between sources and detectors, using a Lagrangian stochastic (LS) model. At issue is whether it is advantageous to recognize the flow as being disturbed and use a computed approximation to that disturbed flow to drive a fully three-dimensional LS model (3D-LS), or whether it suffices to ignore flow disturbance and adopt an LS model attuned to the horizontally homogeneous upwind flow (MO-LS, as Monin–Obukhov similarity theory describes the vertical inhomogeneity). It is demonstrated that both approaches estimate the source strength to within a factor of 2 of the true value, irrespectively of the location of the concentration measurement, and moreover that both approaches estimate the source strength correctly (to within the experimental uncertainty), when based on concentrations measured far away from the immediate influence of obstacles in the flow. However, if the concentration detector is positioned close to the flow-disturbing obstacles, then inverse dispersion based on 3D-LS provides a better estimate of source strength than does MO-LS.

1. Introduction

Consider the challenge of measuring the mean rate Q ($\text{kg m}^{-2} \text{s}^{-1}$) of gas emission to the atmosphere from a localized and uniform near-ground source having a known perimeter—as an example, perhaps one’s interest might be the rate of ammonia volatilization from a small, irregularly shaped plot of soil to which urea fertilizer had been applied, a plot surrounded by untreated soil in an otherwise identical condition. The size of the source is hypothetically too small for practical application of the eddy covariance or flux-gradient approaches. In this situation, presupposing the existence of a suitable model of wind transport, one might invoke the “inverse dispersion”

approach and, instead of directly measuring Q , measure the mean concentration excess C (relative to background) at some convenient downwind point, along with sufficient information to “drive” a meteorological model with whose aid the value of Q necessary to explain measured C is diagnosed.

The idea of inverse dispersion—that is, of inverting the relationship $C = f(Q|\mathbf{u})$ to deduce source strength from known concentration as $Q = f^{-1}(C|\mathbf{u})$ —is both obvious and venerable (note: here $|\mathbf{u}$ signifies that one is given all needed statistics of the turbulent wind field). Flesch et al. (1995) introduced a particularly flexible variant based on the computation of an ensemble of backward-in-time trajectories from detector to source to establish the needed theoretical C – Q relationship (the backward Lagrangian stochastic, or bLS, method). Subsequently, Flesch et al. (2004) demonstrated the bLS method by way of tracer gas trials with a $6 \text{ m} \times 6 \text{ m}$ surface area source in horizontally homogeneous flow designed to establish the

Corresponding author address: J. D. Wilson, Dept. of Earth and Atmospheric Science, University of Alberta, Edmonton, AB T6G2E3, Canada.
E-mail: jaydee.uu@ualberta.ca

level of accuracy that may be hoped for in the best of circumstances¹—a level of accuracy that, incidentally, concurs with the findings of Hanna et al. (1990), who inferred the known source strength of the Project Prairie Grass trials using several dispersion models. The emergence of line-averaging gas detectors having proven opportune for the application of this technique (largely because modeling crosswind spread is more difficult than vertical spread), bLS has now been applied by the present authors and colleagues to estimate gas emissions from confined animal operations, such as hog farms (Flesch et al. 2005a), feedlots (Flesch et al. 2007), and dairies (Flesch et al. 2009). Other applications have been reported by Laubach et al. (2008), Loh et al. (2009), and McGinn et al. (2009).

In the above-cited work the needed theoretical C - Q relationship was provided by a backward Lagrangian stochastic model that represented the wind as being horizontally homogeneous, and described by Monin–Obukhov profiles matched to whatever wind statistics had been measured, usually by a sonic anemometer standing in a region of relatively undisturbed flow. For this reason we here relabel the bLS technique used by previous authors as MO-bLS. Now at some of these sites where MO-bLS has been employed, obstacles such as barns, lagoons, or fences undoubtedly disturbed the flow. An earlier investigation (Flesch et al. 2005b) of MO-bLS in intentionally disturbed winds suggested that, provided the concentration detector was sufficiently remote from the source to ensure that a good fraction of the path from source to detector lay in undisturbed flow, the technique could be applied with adequate accuracy. However, the subjectivity entailed in judging whether a site and instrument setup is adequate exposes MO-bLS to the accusation of failing to represent flow complexity, and criteria addressing the robustness of MO-bLS at imperfect sites are needed.

That, however, is not our main objective here. Instead we examine the advantages and disadvantages of adopting as basis for inverse dispersion a Lagrangian model that recognizes and accommodates the flow disturbance, to the extent that it can be approximated from measurements or a computer simulation: we shall label this approach 3D-LS, and more specifically 3D-fLS or 3D-bLS accordingly as trajectories are computed forward or backward in time. There is no difficulty in principle to adopt 3D-LS for inverse dispersion; however, it is well known that Reynolds-averaged Navier–Stokes (RANS) wind

models are imperfect (e.g., Pope 2000; Leschziner 2000) and so it is an open question as to whether, in practice, source strength inference on the basis of 3D-LS—that is, symbolically $Q = f^{-1}(C|\mathbf{u}_{3D})$ —could be meaningfully more accurate than on the basis of MO-LS. The purpose of this paper, then, is to investigate whether there is a gain in accuracy from adopting 3D-LS over MO-LS for inverse dispersion calculations, in reference to a particular tracer gas dispersion trial that involved a small area source enclosed by a porous shelter fence. The 3D wind field permitting us to address this question stems from earlier simulations by Bourdin and Wilson (2008), using the code Fluent with a k - ϵ turbulence closure.

2. The Ellerslie Tracer Experiment

Figure 1 is a schematic of the Ellerslie tracer gas trials. A porous plastic windbreak fence, of height $h = 1.25$ m and porosity 45% and having resistance coefficient² $k_r = 2.4$, was erected on a uniform plain to shelter a square plot of side length $D = 20$ m. Centered within this plot a PVC manifold (see Fig. 2 of Flesch et al. 2005b) served as a controlled source of tracer methane, released from 36 outlets arranged uniformly over an area of $6 \text{ m} \times 6 \text{ m}$.

A mast standing $10.4h$ west and $0.8h$ south of the southwest corner of the fence carried cup anemometers at heights $z = (0.65, 1.12, 2.12, 3.6, 6.05)$ m and a three-dimensional sonic anemometer, this last at the reference height, $z = z_R = 2.2$ m. These instruments established the state of the surface layer upwind from the plot (i.e., friction velocity u_* , Obukhov length L , mean wind direction β , and roughness length z_0). Identical cup anemometers standing at $z = h/2$ within the plot established the complex pattern of mean wind speed [as reported by Wilson and Flesch (2003), see especially their Fig. 14]; however, anemometers were not operated in the downstream wake of the leeward shelter fence(s). We shall use the convention that mean wind direction β is measured relative to the orientation of the upwind fence; thus $\beta = 45^\circ$ is corner flow, while $\beta = 0^\circ$ is an approach flow normal to the upwind side of the plot. The coordinates will be specified relative to an origin lying at the center of the plot. Throughout the paper, u_* is to be interpreted as the friction velocity in the undisturbed region of the flow.

During the trace gas dispersion trials pairs of open path laser gas detectors (path height $z_L = 1$ m) were operated near the source, either within or downstream from

¹ Broadly interpreted, the findings of Flesch et al. (2004) indicate that even at an ideal site the error in bLS estimates of source strength for an individual run can be as large as of order $\pm 50\%$ – 100% . However, when estimates from numerous runs are compounded, the error converges to a smaller circa 5%.

² In our definition the pressure drop across the material, if blocking a stream of density ρ and uniform normal velocity u , is $\Delta p = k_r \rho u^2$. Please note that Bourdin and Wilson (2008) used the other common convention in which the pressure drop is $(1/2)k_r \rho u^2$; thus, in their terms $k_r = 4.8$.

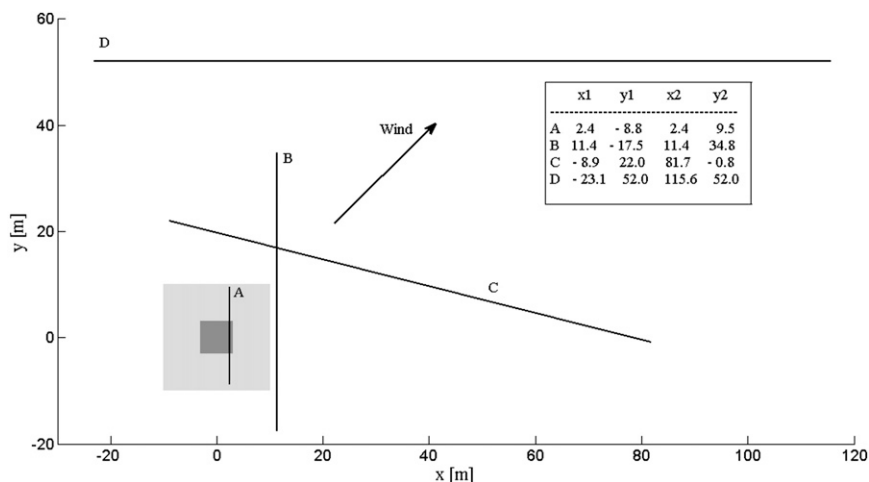


FIG. 1. Configuration of Ellerslie tracer gas experiments: windbreak (larger square; 20-m sidelength), ground-level trace gas source (smaller square; 6-m sidelength), and laser gas detectors A, B, C, D (lines) with pathlengths (18.3, 52.3, 93.4, 138.6) m, respectively. Mean wind direction is aligned with the diagonal. The reference mast stood more than 10h westward (upwind) from the southwest (upwind) corner of the windbreak. The inset table gives coordinates (in meters, relative to plot center) of the two ends of the laser detector, for each configuration.

the sheltered plot. This paper focuses on inverse dispersion relative to four laser paths (Fig. 1), three of which (A, B, D) were parallel with different sides of the plot. Configuration A represents a laser with pathlength 18.3 m traversing the square plot and running over the edge of the gas source. Configuration B is a longer path of 52.3 m, running just outside the shelter plot. Configuration C with pathlength 93.4 m is an oblique path (and is treated here only in backward simulations). Configuration D is a much more distant laser, with pathlength 138.6 m. The laser detectors provided 15-min mean values of line-averaged concentration, while a rotameter monitoring the flow rate from the gas cylinder supplying the source gave the true source strength Q , to within an uncertainty of about $\pm 5\%$. For further details, please refer to Flesch et al. (2004, 2005b).

a. Selection and normalization of experimental data

Numerous 15-min runs were made over several days, providing paired (C , Q) data for each of the above configurations over a range of conditions as regards stratification (Obukhov length L), wind speed, and wind direction (β). Now if S represents the mean horizontal wind speed at $z = 2.2$ m on the reference mast in the undisturbed flow, and if we treat roughness length z_0 as invariant (i.e., common to all runs), then according to the extended Monin–Obukhov similarity theory (e.g., Wilson 2008) the statistical state of the upwind surface layer may be characterized by a quartet of external (or governing) variables, namely (S , β , L , δ), where δ is the boundary layer depth. (Note: here we use the reference wind speed

S in lieu of the friction velocity u_* , which is permissible because the two are in 1:1 relationship for given z_0 .)

For the present study we selected a subset of 15 runs that occurred during effectively neutral stratification ($|L| \geq 150$ m), and for each of which the mean wind direction was almost parallel to the diagonal across the plot ($|\beta - 45^\circ| \leq 5^\circ$). This selection fixes (i.e., holds constant) two of the four external variables. We did not measure the boundary layer depth, which therefore represents an unknown and uncontrolled factor. However, velocity statistics in a neutrally stratified surface layer are relatively insensitive to δ , and so we exploited the expected (approximate) invariance of the dimensionless measured product SC/Q so as to be able to combine together runs that took place with differing mean wind speed to form the average SC/Q for any given configuration. The influence, if any, of varying δ should have been expressed primarily by variation of the normalized horizontal velocity standard deviations $\sigma_{u,v}/u_*$ across the 15 selected runs. Our use of concentration line averages across the plume should to some extent have suppressed the influence of such variations on the dimensionless product SC/Q .

Table 1 gives the available individual values of SC/Q , along with the composite value, for each configuration. By comparing a modeled value $(SC/Q)^*$ with that observed (in the mean) for a given configuration, we can extract the ratio

$$\frac{Q^{LS}}{Q} = \frac{SC/Q}{(SC/Q)^*} \quad (1)$$

TABLE 1. Measured SC/Q (normalized concentration rise above background) for each configuration (S is the mean horizontal wind speed as measured by a sonic anemometer in the approach flow at the reference height $z_R = 2.2$ m). Identifier ID, day, and time cross-reference each run to the fuller description given by Flesch et al. (2005b). Runs have been selected for alignment of the mean wind direction (β) along the diagonal across the plot and for effectively neutral stratification so that, in principle, for each detector SC/Q should be invariant across all runs within a given configuration (A, B, C, or D). For each configuration the average SC/Q is given (in boldface). Alongside, the first number in parentheses is the standard error (se) over the M estimates in the configuration (i.e., standard deviation divided by \sqrt{M}), while the second number is the standard error expressed as percentage of the mean. The latter does not embrace the uncertainty stemming from the gas source strength, which contributes a further nominal $\pm 5\%$ uncertainty in experimental SC/Q .

Configuration	ID	Day	Time	S (m s ⁻¹)	β (°)	u_* (m s ⁻¹)	L (m)	SC/Q
A	F2-5	148	1315	12.85	41	0.88	-198	0.017 76
A	F2-5	148	1330	13.17	40	0.88	-197	0.017 28
A	F2-5	148	1345	12.88	45	0.88	-196	0.019 83
A	F2-5	148	1500	12.45	41	0.85	-207	0.021 00
A	F5-5	152	1515	9.27	42	0.69	-117	0.025 11
A	F5-5	152	1530	8.88	44	0.62	-128	0.025 55
A	F5-5	152	1600	8.70	41	0.64	-190	0.022 45
A	F5-5	152	1615	8.77	47	0.66	-206	0.020 65
A	F5-5	152	1630	9.24	49	0.69	-235	0.026 63
A	F5-5	152	1645	9.60	47	0.73	-232	0.018 68
Avg (se)								0.021 49 (1.1×10^{-3} , 5%)
B	F2-6	148	1315	12.85	41	0.88	-198	0.025 89
B	F2-6	148	1330	13.17	40	0.88	-197	0.025 76
B	F2-6	148	1345	12.88	45	0.88	-196	0.026 12
B	F2-6	148	1500	12.45	41	0.85	-207	0.023 85
Avg (se)								0.025 40 (5.2×10^{-4} , 2%)
C	F5-6	152	1515	9.27	42	0.69	-117	0.007 48
C	F5-6	152	1530	8.88	44	0.62	-128	0.007 17
C	F5-6	152	1600	8.70	41	0.64	-190	0.006 87
C	F5-6	152	1615	8.77	47	0.66	-206	0.007 44
C	F5-6	152	1630	9.24	49	0.69	-235	0.007 27
C	F5-6	152	1645	9.60	47	0.73	-232	0.007 40
Avg (se)								0.007 27 (9.3×10^{-5} , 2%)
D	F6-6	156	1215	5.94	44	0.45	-134	0.001 81
D	F6-6	156	1230	5.46	42	0.42	-103	0.001 40
D	F6-6	156	1400	5.40	43	0.42	-100	0.002 11
D	F6-6	156	1415	6.22	43	0.48	-118	0.002 14
D	F6-6	156	1430	6.66	43	0.47	-151	0.002 22
Avg (se)								0.001 94 (1.5×10^{-4} , 8%)

of inferred-to-true source strength (note: each of the detector configurations was used independently to deduce Q). Similarly in the practical application of the technique, the desired value of the unknown source strength would be obtained as

$$Q^{LS} = \frac{SC}{(SC/Q)^*} \tag{2}$$

b. Micrometeorological constants

Simulations to establish the normalized concentration $(SC/Q)^*$ may be performed with any specification of the overall wind speed (as characterized by S or equivalently by the friction velocity u_*), because in the high-Reynolds-number flows characterizing the atmospheric boundary layer, the computed SC/Q product is insensitive to its choice (and there is no explicit role for the

boundary layer depth δ in a Fluent-RANS simulation of the surface layer). However, it is desirable to have the simulations reproduce particular values of certain key dimensionless variables observed by the sonic anemometer (at reference height $z = z_R = 2.2$ m) in the undisturbed flow region: namely, the ratio S/u_* of mean horizontal wind speed to friction velocity, and the ratios $c_{u,v,w} = \sigma_{u,v,w}/u_*$ of velocity standard deviation to friction velocity, ratios which together fix the (normalized) turbulent kinetic energy, as $E/u_*^2 \equiv (c_u^2 + c_v^2 + c_w^2)/2$. To accomplish this attuning of the computed flow to the observations, our starting point was to choose representative values for the sonic anemometer observations during neutral conditions. Accordingly we have set $c_{u,v,w} = (2.8, 2.4, 1.1)$, which implies $(E/u_*^2)^{exp} = 7.41$, and assumed for S/u_* the value $[k_v^{-1} \ln(z_R/z_0)]$ that is implied by the roughness length as cited by Wilson and Flesch (2003): namely, $z_0^{exp} = 0.015$ m (here k_v is the von Kármán

constant, whose value we assume is $k_v = 0.4$; we are using “exp” to indicate experimental values of key micrometeorological variables). Note that with $c_w = 1.1$ we have a smaller value of σ_w/u_* than is often cited, but we have no reason to disbelieve it (see Wilson 2008).

3. The Lagrangian stochastic model

Trajectories were computed using the Thomson (1987) well-mixed three-dimensional model for Gaussian inhomogeneous turbulence. The general setup of the algorithm follows that detailed by Wilson et al. (2009), who had applied the Thomson model to compute trajectories in urban flow. The present code is simpler in that it need not deal with excluded volumes (buildings), but otherwise the prescription given by Wilson et al. covers the present simulations and we need not elaborate. The flow properties required by the trajectory algorithm as inputs are the mean velocity vector \bar{u}_i , the Reynolds stress tensor $R_{ij} \equiv \overline{u'_i u'_j}$, and the turbulent kinetic energy dissipation rate ϵ . Please note that we reserve symbols $U_i = (U, V, W)$ for the components of the Lagrangian velocity fluctuation relative to the local Eulerian mean velocity $\bar{u}_i = (\bar{u}, \bar{v}, \bar{w})$, while u'_i is the vector of Eulerian velocity fluctuations.

a. Specification of the Kolmogorov constant

Thomson’s model requires a specification of a Kolmogorov constant C_0 , this being the only parameter that can be regarded as flexible. Wilson et al. (2009) discuss this choice at length, noting the choice amounts (implicitly) to a tuning of the Lagrangian model so as to implement (again, implicitly) a target value for the turbulent Schmidt number (S_c). For the reasons given in that paper, here we assumed $S_c = 0.63$ and specified the Kolmogorov constant as

$$C_0 = 2S_c(c_w^4 + 1), \quad (3)$$

where c_w is the chosen value for σ_w/u_* in the approach flow. As noted above we set $c_w = 1.1$ (on the basis of observations from the sonic anemometer in the upstream flow region), thus for the Lagrangian simulations of this paper $C_0 = 3.10$.

b. Time scale and time step

Given a specified field of velocity statistics and a prescribed C_0 , Thomson’s LS model produces an ensemble of trajectories to which one might like to impute a velocity decorrelation time scale—but one does not explicitly prescribe that property, in the sense of imposing it as an input or “driving” property. Like Wilson et al. (2009) we regard the derived (or secondary) quantity

$$\tau = 2\sigma_w^2(C_0\epsilon)^{-1} \quad (4)$$

as being an effective time scale (thus the label, τ), and assume it is of the same order of magnitude as the velocity autocorrelation. We required that the time step Δt satisfy $\Delta t \ll \tau$. We also required that the time step be small with respect to an inhomogeneity time scale

$$\tau_h = \frac{\sqrt{\Delta x^2 + \Delta y^2 + \Delta z^2}}{\sqrt{(U + \bar{u})^2 + (V + \bar{v})^2 + (W + \bar{w})^2}}, \quad (5)$$

which characterizes particle transit time across the grid cell (of dimension $\Delta x \times \Delta y \times \Delta z$). Therefore we specified

$$\Delta t = \mu \min(\tau, \tau_h), \quad (\mu \ll 1). \quad (6)$$

How small does μ need to be? The physical source in the Eilerslie tracer experiments having been at ground level, backward simulations reported in this work are intended specifically to compute particle residence time in a thin ground-based slab over the (physical) source. Earlier experience (Flesch et al. 1995; Wilson 2007; Cai et al. 2008) suggests that when estimating the C/Q ratio very near the reflecting surface (as opposed to releasing particles from a ground-level source for a forward simulation to detectors away from the ground) it is necessary that the time step be very small; for example, Flesch et al. (1995) set $\Delta t/\tau = 0.025$. The present simulations used $\mu = 0.01$, but differ negligibly from those with a coarser time step ($\mu = 0.05$).

c. Forward and backward simulations performed

If the $C-Q$ relationship $(SC/Q)^*$ is to be determined by reference to an ensemble of random trajectories between source and detector, that ensemble may (according to the user’s preference) entail either forward- or backward-in-time trajectories. In the case that the source has finite volume (or area), backward trajectories are very convenient (for the reasons given by Flesch et al. 1995). However, an equally common case is the continuous point source, and unless one wishes to approximate the point with a finite volume, this necessitates the forward approach. In short, each approach (i.e., forward, backward) is apt for a certain circumstance, and so both are necessary. However, our reason for examining both approaches here is more fundamental than the mere utility of each, in that we wish to demonstrate (or confirm) their equivalence. That point is less central to our paper than the key question of the relative accuracies of 3D-LS and MO-LS for inverse dispersion in a disturbed flow, and so it is relegated to the appendix.

d. Configuration of sources and detectors

Information on mean concentration is most easily extracted from an ensemble of trajectories by computing the mean particle residence time within a finite volume detector, and it is important in the present context to carefully prescribe its dimensions. Except for those simulations described in the appendix (simulations which, as explained above, were intended to examine consistency of forward and backward treatments) the backward simulations treated the lasers as line sources (the importance of this is discussed in the appendix). Bearing in mind the likelihood of strong vertical concentration gradients near ground over the (physical) source, it was important that the backward residence time detector be shallow, and be centered near $z = z_0$. This was achieved by using the touchdown counter method; namely, for each set (or subensemble) of computed paths the C/Q ratio was computed as

$$\frac{C}{Q} = \frac{1}{N_P} \sum_k \frac{2}{|w_{0k}|}, \quad (7)$$

where w_{0k} is the vertical velocity upon the k th particle reflection off ground ($z = z_0$) within the perimeter of the source, and N_P is the number of backward paths computed in each of $N = 19$ subensembles. This estimator is equivalent to computing mean particle residence time in a layer of arbitrarily small depth covering the source. [Regarding the index k , please note that any one particle may reflect off ground many times, and that every such reflection occurring within the boundary of the source contributes to the summation in Eq. (7).]

e. Initial velocity, surface reflection, and velocity limit

For a particle about to be released within the grid cell indexed (I, J, K) the velocity fluctuation components were initialized as

$$W = \sigma_w r_w, \quad (8)$$

$$U = \sigma_u (\alpha_{uw} r_w + \sqrt{1 - \alpha_{uw}^2} r_u), \quad \text{and} \quad (9)$$

$$V = \sigma_v (\alpha_{vw} r_w + \sqrt{1 - \alpha_{vw}^2} r_v), \quad (10)$$

where the r_i are independent standardized Gaussian random numbers, $\alpha_{uw} = \overline{u'w'}/(\sigma_u \sigma_w)$ (etc.) are the velocity correlations, and all velocity statistics were given the values pertaining to the node in the release cell. If a particle's displacement during $t^n \rightarrow t^{n+1}$ ($=t^n + dt$) took it below the level z_0 , that is, the provisional particle height $Z^*(n + 1)$ at time $n + 1$ lay below the roughness height, it was subjected to perfect reflection:

$$Z(n + 1) = 2z_0 - Z^*(n + 1), \quad (11)$$

$$W(n + 1) = -W^*(n + 1), \quad (12)$$

$$U(n + 1) = -U^*(n + 1), \quad \text{and} \quad (13)$$

$$V(n + 1) = -V^*(n + 1). \quad (14)$$

Thus all components of the Lagrangian velocity fluctuation were reversed upon reflection, as is required to preserve the velocity covariance.

Yee and Wilson (2007) noted that, when driven by a disturbed flow field, the present LS algorithm [originating with Thomson (1987)] may generate excessively large velocities. Like Wilson et al. (2009), we imposed a limit ($U_i \leq 6\sigma_{u_i}$) on the permitted magnitude of the Lagrangian velocity fluctuations U_i ; if this limit was exceeded by any component, all velocity fluctuations were reset by making a random choice from the local Eulerian velocity distribution. In simulations treating the flow as horizontally uniform, such rogue velocities, if they occurred at all, occurred but once or twice. As for rogue velocities in the disturbed flow, in a particular forward simulation of $19 \times 16\,000$ forward paths with $\mu = 0.01$, the Gaussian random number generator was sampled more than 3×10^9 times to compute the vertical velocity component (3 times that figure in total), while velocity fluctuations exceeding the 6σ level occurred only 67 times.

4. The discretized (gridded) flow field

This paper will report LS-based inverse dispersion inferences of source strength based comparatively on horizontally uniform winds (MO-LS), or based on a computed field representing the (actually) disturbed wind (3D-LS). But irrespectively of whether it was treated as horizontally-homogeneous or otherwise, the flow field driving the LS model was represented on a stretched, three-dimensional Cartesian grid³ covering a very large domain with sidelengths $(X, Y, Z) = (96, 96, 41)h$, centered on the middle of the plot. Within this domain, the flow was stored at $123 \times 123 \times 34 = 514\,386$ nodes. Thus

³The flow fields had been computed by Bourdin and Wilson (2008) using a collocated "O-topology grid," with 454 272 nodes. Full details are given by Bourdin and Wilson (their section 4.1), and of most relevance here, the volume within the windbreak was uniformly discretized into 10 cells along its $h = 1.25$ m height and 80 cells along its $D = 20$ m sidelength, while outside that core region a stretching ratio of 1.2 was applied (from the interior toward the exterior of the domain). The computed wind field was interpolated from Fluent's grid onto the Cartesian mesh used for the trajectory simulation; within the confines of the windbreak the mesh intervals were $\Delta x/h \equiv \Delta y/h = 0.2$, $\Delta z/h = 0.1$.

the flow field was discretized, which usually is not the case in the context of Lagrangian stochastic models.

The implications of this are subtle, and not entirely clear. The grid length near ground ($\Delta z = h/10 = 0.125$ m) vastly exceeded the roughness length ($z_0 = 0.015$ m) and so, with Eq. (6) ensuring that (with $\mu \ll 1$) many steps are required to move from one cell to another, flow statistics (sampled by the traveling particle) are almost always invariant from one step to the next (note: in these simulations we did not interpolate velocity statistics from the nearest nodes to the particle position). This should mitigate to some extent the (already small) Δt bias error of the trajectory model (Wilson and Flesch 1993), and possibly also mitigate any loss of accuracy because of the imposition of perfect reflection: because flow statistics are height-invariant across the lowest cell and thus local homogeneity applies.

a. Quality of the computed flow field

The realizable $k-\epsilon$ closure (rke) used by Bourdin and Wilson (2008) is one of the many variants of two-equation closure, wherein closure is attained by introducing an eddy viscosity based on \sqrt{E} as velocity scale and E/ϵ as time scale (generally the constants of proportionality are constrained to reproduce the known eddy viscosity $k_v \mu_{*z}$ of a neutral wall shear layer). Many authors have written concerning the virtues and deficiencies of this class of closure, and it will suffice for our purposes to appeal to surveys. Leschziner (2000) notes that $k-\epsilon$ closures “often perform poorly in high curvature, separation, recirculation, impingement and swirl.” Similarly Pope (2000), surveying the accuracy of two-equation turbulence closures, notes that the $k-\epsilon$ closure may perform poorly in three-dimensional flows and/or in strong pressure gradients. The windbreak flow considered here is three-dimensional and involves strong pressure gradients (Wilson 1997) and associated streamline curvature (Plate 1971). The paired vortices induced in corner flow (observed by Richards 1986, using smoke and tufts) suggest “swirl.” Thus it may be unrealistic to consider this flow as being amenable to highly accurate simulation by the RANS class of turbulence closure.

Nonetheless Fig. 2, reproduced from Bourdin and Wilson (2008) and giving the computed mean velocity on a transect along the diagonal at $z/h = 1/2$ in comparison with observations, indicates the simulated flow field is rather realistic in terms of capturing the amplitude of the spatial variation in mean wind speed. A cursory examination of other model transects of wind speed did not reveal any objectionable features, and the overall pattern (see Bourdin and Wilson 2008, Fig. 15) strongly resembles that observed (Wilson and Flesch 2003, Fig. 14). Figure 3 bears on the quality of the computed turbulence

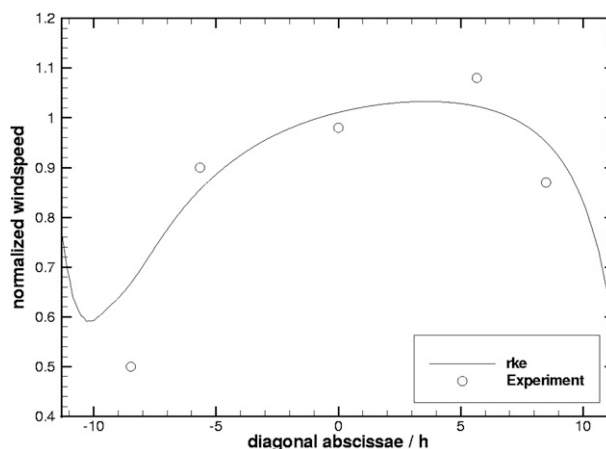


FIG. 2. Transect of normalized mean cup wind speed S/S_0 at height $z/h = 1/2$, along the diagonal of the square sheltered plot, during corner flow. Line is the Fluent simulation using the rke closure (Bourdin and Wilson 2008), while \circ symbols are cup anemometer observations (Wilson and Flesch 2003).

statistics, and again, is satisfactory at the qualitative level. Based on what is known of turbulence in the wake of windbreaks (e.g., Raine and Stevenson 1977), the computed pattern of turbulent kinetic energy (Fig. 4) also appears to be satisfactory (however no measurements were made in the downstream region of the present flow). It would be surprising, however, if the turbulence statistics provided by the simulation were true at every point in the flow domain (even at the 10%–20% level of accuracy), witness Wilson’s (2004) study of windbreak simulations, or that of Santiago et al. (2007) who compared the performance of three variants of $k-\epsilon$ closure in Fluent simulations of windbreak flow and noted “performance of any of these models against the wind tunnel data is not particularly good.”

Lest the tone of the preceding paragraphs seems unduly cautious or even pessimistic, we close this section by stressing the qualitative resemblance of the modeled and measured flows. In any case, the results to follow indicate that a computational model of a disturbed wind field need not be perfect in order to be useful in the context of (inverse) dispersion.

b. Rescaling the computational flow

The Fluent computations by Bourdin and Wilson (2008) treated the flow as unstratified, a good approximation for the experimental runs considered in this paper (for which the Obukhov length $|L| \geq 150$ m), with the friction velocity at the inflow boundary fixed at $u_*^F = 0.4$ m s $^{-1}$ and the roughness length specified as $z_0^F = 0.015$ m, the value reported by Wilson and Flesch (2003). The simulation provides the fields of mean velocity \bar{u}_i , of the turbulent kinetic energy E and its dissipation rate ϵ , and of

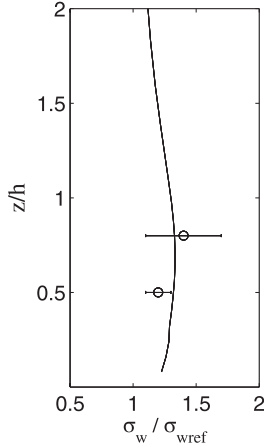


FIG. 3. Fluent's computed profile at the plot center of normalized standard deviation of vertical velocity vs observations (with range) from sonic anemometers (h is the windbreak height). Values are normalized on the reference value (of σ_w) at $z = z_R = 2.2$ m in the upwind flow.

the shear stresses $\overline{u'w'}$, and so on. For clarity, we append a superscript F to identify the “raw” computed values—for example, $\overline{u}_i^F(I, J, K)$ is the Fluent field of the mean velocity—and we note the distinction between directional indices, such as appear in the velocity vector $\overline{u}_i^F \equiv (\overline{u}^F, \overline{v}^F, \overline{w}^F)$, and the (upper case) indices (I, J, K) that we use to label the coordinates of the grid nodes.

Having decided to focus on modeled $(SC/Q)^*$, that is, a dimensionless ratio, there was no need to adjust the Fluent fields in terms of the overall velocity scale. However, we did uniformly rescale the Fluent fields to reproduce the aforementioned values (section 2b) of key dimensionless variables observed by the reference sonic anemometer at height $z = z_R = 2.2$ m in the upwind flow. Let K_R be the height index for nodes whose height corresponds most closely to the height of the reference sonic anemometer, and let I_0, J_0 be the indices associated with the horizontal coordinates of the southwest corner of the grid. Then (I_0, J_0, K_R) represents the farthest upwind node at the height of the sonic anemometer, and is positioned in the undisturbed flow. Now let $\hat{E}^F \equiv E^F(I_0, J_0, K_R)$, $\hat{\epsilon}^F \equiv \epsilon^F(I_0, J_0, K_R)$, $\hat{u}^F \equiv \overline{u}^F(I_0, J_0, K_R)$ represent Fluent's solution for the numeric values at node (I_0, J_0, K_R) of respectively the TKE, the dissipation rate, and the x component of mean velocity, and so on. The desired rescaling was accomplished by basing the 3D-LS calculation on the adjusted fields

$$\overline{u}(I, J, K) = \overline{u}^F(I, J, K) \frac{k_v^{-1} \ln(z_R/z_0)}{\hat{u}^F/u_*^F}, \quad (15)$$

$$\overline{v} = \overline{v}^F \frac{k_v^{-1} \ln(z_R/z_0)}{\hat{v}^F/u_*^F}, \quad (16)$$

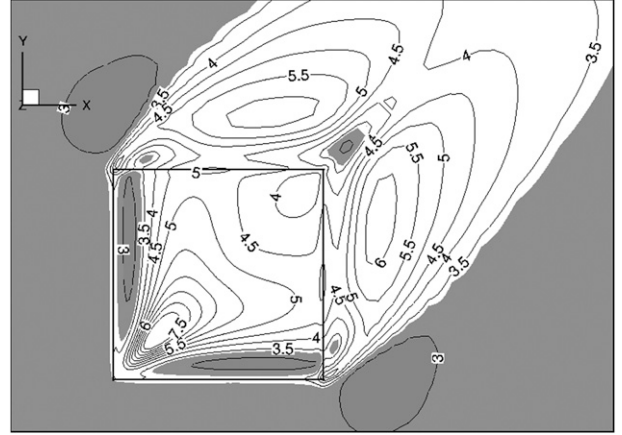


FIG. 4. Contours of normalized turbulent kinetic energy $E^F/(u_*^F)^2$, as computed by Fluent (u_*^F being the friction velocity in the upstream region). The upstream value (as prescribed in the simulations) was $E/u_*^2 = 3.3$. For the Lagrangian simulations we rescaled the Fluent field E^F so that the value at the reference sonic matched the observed value, $(E/u_*^2)^{\text{exp}} = 7.4$.

$$\overline{w} = \overline{w}^F \frac{k_v^{-1} \ln(z_R/z_0)}{\hat{w}^F/u_*^F}, \quad (17)$$

$$E = E^F \frac{(E/u_*^2)^{\text{exp}}}{\hat{E}^F/(u_*^F)^2}, \quad (18)$$

$$\epsilon = \epsilon^F \frac{(k_v z_R)^{-1} (u_*^F)^3}{\hat{\epsilon}^F}, \quad (19)$$

$$\overline{u'^2} = \frac{2c_u^2}{c_u^2 + c_v^2 + c_w^2} E, \quad \text{and} \quad (20)$$

$$\overline{u'w'} = (\overline{u'w'})^F \quad (21)$$

[other components of the stress tensor follow the indicated pattern; and for brevity the spatial indices I, J, K have been suppressed in Eqs. (16)–(21)]. The rescaling factor for the mean velocities [i.e., fraction on the right-hand sides of Eqs. (15)–(17)] was 1.05 (the ratio of Fluent's specification for the von Kármán constant and our own specification $k_v = 0.4$), while the rescaling factors for turbulent kinetic energy and its dissipation rate were respectively 2.27 and (again) 1.05. (Explanation: the property E/u_*^2 is not universal across adiabatic wall shear layers, and the Fluent simulation had set this as 3.33, whereas our neutral experiments suggested a mean value of 7.41.) After the above adjustments, the field of the kinematic shear stress tensor $\mathbf{R} = R_{ij} = \overline{u'_i u'_j}$ was checked for violations of Schwartz inequality

$$(\overline{u'_A u'_B})^2 \leq \sigma_A^2 \sigma_B^2 \quad (A \neq B); \quad (22)$$

however, no such violations were found.

In the upstream region these rescaled computational wind statistics closely represent the experimental flow (exactly so, at the reference height), while in the region of the flow disturbance the results of Bourdin and Wilson (2008), shown earlier, are indicative.

c. Overwriting a horizontally homogeneous flow onto the grid

Because we are interested in the comparative performance of LS simulations (and performance for inverse dispersion) with and without making allowance for (or recognizing) flow disturbance, it was necessary for the MO-LS simulations to overwrite the Fluent-derived flow field. In this case, bearing in mind our focus on the property SC/Q , which is invariant relative to the velocity scale (which may be taken, equivalently, to be either S or u_*), we adopted the dimensionless properties of the flow as described in section 2b and that summarize the observations of the sonic anemometer. From those properties we wrote onto the grid a horizontally uniform flow:

$$\bar{u}(I, J, K) = \frac{1}{\sqrt{2}} \frac{u_*^F}{k_v} \ln \frac{z(K)}{z_0}, \quad (23)$$

$$\bar{v} = \frac{1}{\sqrt{2}} \frac{u_*^F}{k_v} \ln \frac{z(K)}{z_0}, \quad (24)$$

$$\bar{w} = 0, \quad (25)$$

$$E = \frac{c_u^2 + c_v^2 + c_w^2}{2} (u_*^F)^2, \quad (26)$$

$$\epsilon = \frac{(u_*^F)^3}{k_v z(K)}, \quad (27)$$

$$\overline{u'^2} = c_u^2 (u_*^F)^2 (\text{etc.}), \quad (28)$$

$$\overline{u'w'} = \overline{v'w'} = -\frac{1}{\sqrt{2}} (u_*^F)^2, \quad \text{and} \quad (29)$$

$$\overline{u'v'} = 0. \quad (30)$$

Full spatial indices (I, J, K) have been shown only in the first equation, and of course all these velocity statistics (intended for MO-LS simulations) are invariant with respect to the horizontal indices I, J ; some vary (discretely) with height, through $z(K)$.

5. Results

Recall that the objective is to estimate the strength Q of the $6 \text{ m} \times 6 \text{ m}$ surface methane source, from each given

average concentration excess C . This entails performing a trajectory simulation for each source–detector configuration (A, \dots, D) to extract a theoretical (symbolized $*$) value for the normalized C/Q ratio—that is, for $(SC/Q)^*$. There are four experimental values of SC/Q , and from each pair $[SC/Q, (SC/Q)^*]$ we have an implied value for Q^{LS}/Q , which gives the accuracy with which source strength has been diagnosed by inverse dispersion based on a Lagrangian stochastic calculation of trajectories.

In the simulations to follow each cited value of $(SC/Q)^*$ is the average over $N = 19$ independent subensembles of paths. Stated percentage errors of each simulation, which have been rounded up to whole numbers, represent a normalized standard error; they are defined $\text{se}\% \equiv 100\sigma/\sqrt{N}$, where σ is the standard deviation of $(SC/Q)_1, \dots, (SC/Q)_N$ —that is, over the N subensembles of paths. The number N_P of paths computed within each subensemble was $N_P = 32\,000$ for configurations (A, B) and $N_P = 64\,000$ for configurations (C, D).

a. Concentration field

The one-dimensional (Monin–Obukhov) and three-dimensional (windbreak) flow fields differ radically, and Fig. 5 indicates that, not surprisingly, so too do the corresponding concentration fields, as revealed in concentration contours plotted at the height of the laser detector light paths ($z = 1 \text{ m}$). The concentration field of Fig. 5 has been computed from forward trajectories, on the basis of particle residence times in cells of area $0.25 \times 0.25 \text{ m}^2$ and depth 0.1 m . The irregularity of the contours is stochastic, while the slightly imperfect reflection symmetry (of the contours about the diagonal) visible in Fig. 5 stems from the interpolation of wind statistics from Fluent's grid onto the grid used to compute trajectories.

The difference between the $(SC/Q)^*$ fields indicated by Fig. 5 seems physically plausible, the more so in view of Fluent's decent estimation of the field of mean wind speed (Fig. 2). In the MO velocity field (upper panel of Fig. 5), the contours of SC/Q delineate a narrow plume, elongated in the direction of the mean wind; whereas, in the actual flow (or rather, Fluent's approximation to it) the plume is wider in the crosswind direction and less elongated: the region of high concentrations is in closer proximity to the source. Evidently, then, the laser line-average concentrations must differ from flow to flow.

b. Comparative performance of 3D-bLS and MO-bLS

Table 2 and Fig. 6 compare the performance of MO-bLS versus 3D-bLS for the inference of the source strength, where in both cases $(SC/Q)^*$ has been computed from the touchdown method [Eq. (7)] applied to

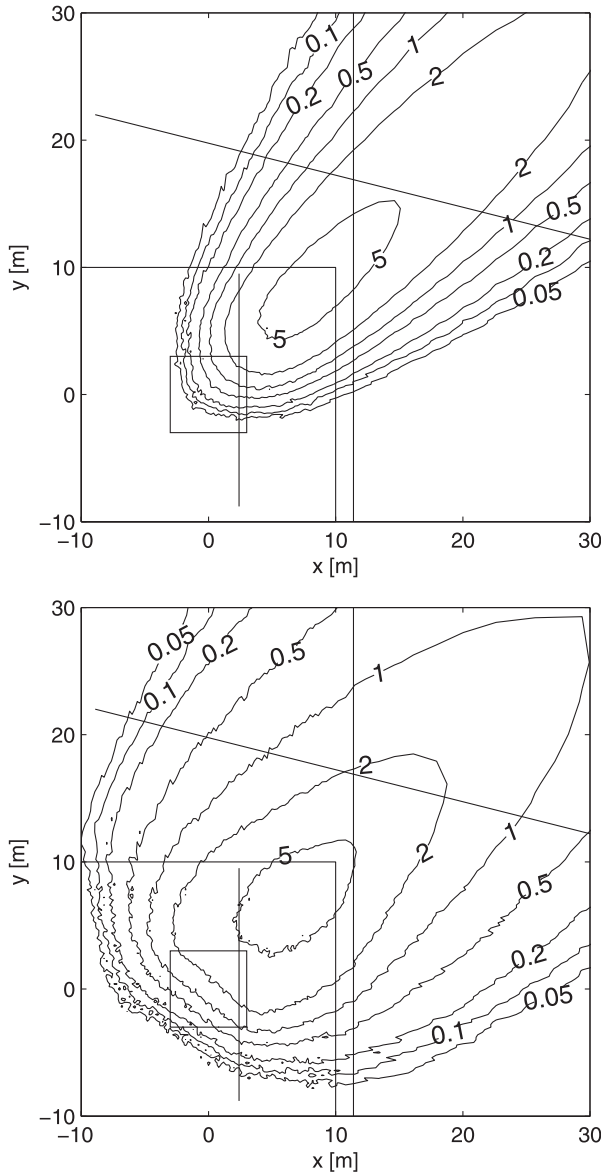


FIG. 5. Computed contours of $(100 \times)$ the normalized concentration SC/Q in the x - y plane at height $z = 1$ m, the height of operation of the laser gas detectors. (top) MO-fLS; (bottom) 3D-fLS. The small square outlines the Ellerslie methane source; the larger square outlines the shelter fence. Other lines show three of the four laser detector configurations (cf. Fig. 1), the fourth (D) lying outside the given view (which truncates the lower end of laser B and the right end of laser C).

backward simulations. (Interested readers may consult the appendix for corresponding results from forward simulations; however, those simulations compromise the experiment by having to represent the detectors with finite cross section. The point of the appendix is strictly to confirm the forward-backward symmetry of the trajectory algorithm.)

TABLE 2. Ratios Q^{bLS}/Q for each configuration indicate the skill with which the inverse dispersion approach has diagnosed source strength from a single measured concentration. Also listed are measured and simulated values of normalized, line-averaged tracer concentration (the reference velocity scale S being the mean wind speed at $z = z_R = 2.2$ m in the upwind flow). For cases denoted “3D,” wind statistics were treated as disturbed, and represented by Fluent’s k - ϵ flow calculation (3D-bLS); otherwise, wind statistics were horizontally homogeneous and represented by Monin-Obukhov profiles (MO-bLS). Numbers in parentheses are the standard errors, expressed as a percentage: these quantify run-to-run variability in the measured value $(SC/Q)^{\text{obs}}$, and stochastic variability in the computed value $(SC/Q)^*$, respectively. In the final column these errors are summed with the uncertainty ($\pm 5\%$) in true source strength, to characterize the overall percentage uncertainty in Q^{bLS}/Q .

		$(SC/Q)^{\text{obs}}$	$(SC/Q)^*$	Q^{bLS}/Q
A	MO	2.15×10^{-2} (5%)	1.20×10^{-2} (3%)	1.80 (13%)
B	MO	2.54×10^{-2} (2%)	1.35×10^{-2} (3%)	1.88 (10%)
C	MO	7.27×10^{-3} (2%)	6.04×10^{-3} (4%)	1.20 (11%)
D	MO	1.94×10^{-3} (8%)	2.22×10^{-3} (4%)	0.87 (17%)
A	3D	2.15×10^{-2} (5%)	2.41×10^{-2} (2%)	0.89 (12%)
B	3D	2.54×10^{-2} (2%)	1.53×10^{-2} (2%)	1.67 (9%)
C	3D	7.27×10^{-3} (2%)	4.93×10^{-3} (4%)	1.47 (11%)
D	3D	1.94×10^{-3} (8%)	1.62×10^{-3} (4%)	1.20 (17%)

For configuration A, where the laser stood within the windbreak and just over the edge of the source, 3D-bLS provides a definitive improvement relative to inference by MO-bLS. In the other three configurations, however, the situation is not so clear cut. Inference by 3D-bLS is marginally better than by MO-bLS at location B, but elsewhere (C, D) it is marginally worse. Overall it is not, then, as clear as one might wish that adopting the more rigorous (albeit imperfect) three-dimensional description of the wind field has proven a better basis for inverse dispersion than the assumption or imposition of a fictitious, undisturbed and horizontally uniform flow.

Be that as it may, the most important point to be made in regard to these results is the fact that, irrespectively of whether one invokes 3D-bLS or the far simpler MO-bLS, all of these inferred Q^{bLS}/Q ratios lie within a factor of 2 of unity: $1/2 \leq Q^{\text{bLS}}/Q \leq 2$. This is indicative of the robustness of inverse dispersion, even where disturbance to the flow is illegitimately (in principle) ignored or imperfectly compensated for; and therein lies the striking utility of the approach. It is also important to recognize that, where applied to the most distant laser (D), both methods have correctly estimated the source strength, bearing in mind the prevailing uncertainties. We do not interpret the $Q^{\text{bLS}}/Q = (1.2 \pm 0.20)$ from 3D-bLS applied to configuration D (see Table 2) as being significantly different from, or worse than, the $Q^{\text{bLS}}/Q = (0.87 \pm 0.15)$ obtained by MO-bLS applied in the same configuration. Such an interpretation would be unwarranted given the prevailing uncertainties, namely,

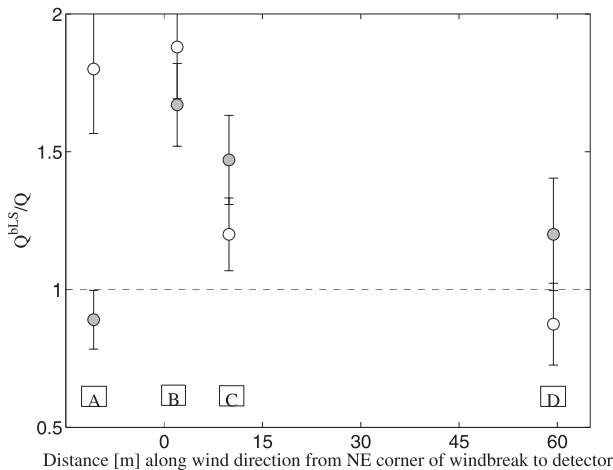


FIG. 6. Performance of inverse dispersion by bLS for the Ellerslie square plot tracer trials, in neutrally stratified corner flow. Open symbols, MO-bLS; filled symbols, 3D-bLS. Uncertainty bars are \pm the sum of uncertainty in true Q , run-to-run variation in $(SC/Q)^{exp}$, and stochastic error in modeled $(SC/Q)^*$. [Notes: Recall that the wind direction is oriented along the diagonal of the plot. For configuration A, the laser detector, standing *inside* the sheltered plot, is *upwind* from the origin of the distance axis used on this diagram (only)—that origin being the NE, i.e., downwind, corner of the plot. Detector B stood just outside the shelter. As regards a scale for distance, the distance from plot center to (any) corner is $\sqrt{200} = 14.1$ m.]

uncertainty in the rotameter's estimation of true emission rate Q , standard error of experimental values of SC/Q across all runs in a given configuration and the statistical indeterminacy inherent in the outcome of the simulations.

c. Interpretation

Referring again to Fig. 5 and configuration A (laser within the windbreak, near the edge of the source), it is clear from the $(SC/Q)^*$ contours that this laser would have detected a much greater line-average concentration in the disturbed (i.e., actual) flow, than had the upwind flow prevailed (undisturbed) over the entire area. Confirming this, from Table 2 we note that laser A in undisturbed flow would see $SC/Q \approx 0.012$ while in the actual flow (or rather, Fluent's approximation to it) laser A would see a twofold higher level $SC/Q \approx 0.024$. The latter is much closer to the measured figure, namely, $SC/Q \approx 0.021$, and so it is clear why, with the laser in configuration A, the source strength is much better estimated by 3D-LS than by MO-LS. The situation is not so clear cut for the other configurations, but probably in the case of configuration B it might be expected (on the basis of Fig. 5) that a laser in the undisturbed (MO) flow would detect a lower SC/Q (see Table 2) than occurred in the actual (disturbed) flow, so that MO-bLS based on configuration B would (again) overestimate the source strength.

6. Conclusions

We have given a rather exhaustive description of the tracer experiment and our subsequent analysis, in case others should wish to improve upon it. It would be of interest to know whether eventual refinement in the technique of micrometeorological wind simulation might provide an improved representation of this disturbed flow, and (in consequence) a demonstrably improved performance of 3D-bLS for all configurations of the detector.

On the other hand one might well ask, given the infinite variety of (possible) disturbances to the wind, what generality could attach to a study of inverse dispersion in this particular case? In that regard, we can only emphasize that this is, anyway, a *strongly* disturbed flow, entailing strong streamwise pressure gradients (up to several pascals over a distance of a few meters; Wilson 1997) and associated strong streamline curvature, and that it is very much a three-dimensional flow. Taken in combination with the study of Wilson et al. (2009), it would appear (from the definitive superiority of 3D-LS for configuration A) that evidence for the advantage of 3D-LS in computing the C - Q relationship is accumulating (there would be little point in the enterprise of developing micrometeorological wind models, were that not the case). As foreshadowed earlier, the present results indicate that a computed flow field need not be perfect in order to be useful.

However, if one decides to perform inverse dispersion based on a representation of the flow as being disturbed (RANS wind model \rightarrow 3D-LS),⁴ then complications ensue that to some extent compromise any hope for a greater objectivity than attaches to the simpler approach we have labeled MO-LS—that is, the approach of treating the flow as undisturbed, and positioning detectors so as to minimize the influence of that disturbance. Computing a disturbed wind field is onerous, demands specialized expertise, and entails arbitrary choices: of turbulence closure; of closure parameters; of micrometeorological parameters (such as $c_u = \sigma_u/u_*$); of spatial resolution ($\Delta x, \Delta y, \Delta z$); and more. Particularly if the flow is stratified (as in general it must be), the coupling of the velocity statistics to temperature and even humidity statistics proliferates the number of quantities needing to be specified as boundary conditions in order to respect the surface energy balance. And as if those complications were insufficient, one needs also to implement a much more complex model of trajectories.

⁴ One could also have performed inverse dispersion using an Eulerian treatment, which would offer the efficiency of being able to be handled simultaneously with the wind calculation. However, the tracer calculation necessarily is specific to each source configuration, and the latter may sometimes need to be treated as unknown.

The MO-bLS approach to inverse dispersion is simple, flexible, and rapid—able to provide a first estimate of source strength for any given interval within hours (easily) and (if need be) in a matter of minutes, after the required measurements are made. On the evidence of this paper the more complex approach of 3D-bLS does potentially afford a systematic improvement in accuracy if the detector must be placed in a region of very disturbed winds. Nevertheless, we recommend that the bLS approach to inverse dispersion should normally be based on the approximation of an undisturbed flow, with detectors appropriately placed so as to reduce the sensitivity of the C/Q ratio to whatever flow disturbance does actually arise. We have yet to encounter an example of MO-bLS, applied in this spirit and with appropriate criteria regarding data quality (proper accounting of experimental uncertainties) and atmospheric state (definitively measured, and not too extreme), yielding an estimate of source strength (deduced from crosswind line-averaged concentration) that is wrong, in the mean over numerous trials, by worse than about $\pm 20\%$.

Acknowledgments. This work was funded by grants from the Natural Sciences and Engineering Research Council of Canada (NSERC) and the Canadian Foundation for Climate and Atmospheric Sciences (CFCAS). We received helpful input from three anonymous reviewers.

APPENDIX

Forward–Backward Consistency of the LS Simulations

Except from the influence of discretization error and the intervention of a reflection algorithm at boundaries, forward and backward Lagrangian stochastic models ought to provide identical estimates of the ratio “ C/Q ,” that is, the mean concentration averaged over the volume of the detector D caused by unit release per unit time within the volume of the distributed source S. It is important that we here correct a mistaken suggestion of Wilson et al. (2009, footnote, p. 1595) that forward and backward LS models may provide severely inconsistent estimates of C/Q in this highly disturbed shelter flow. The preliminary simulations of the square plot flow briefly alluded to in that paper are invalid, having been contaminated by an unsuspected error in the computation of Reynolds stress gradients in the flow field (missing brackets).

That coding error corrected, the present simulations based on disturbed flow satisfactorily uphold forward–backward symmetry. To test the question, it was important to treat sources and detectors consistently across

TABLE A1. Comparing forward (f) and backward (b) simulations, the lasers being treated as (equal) finite volume detectors (forward) and sources (backward). For cases denoted “3D” wind statistics were treated as disturbed, and represented by Fluent’s $k-\epsilon$ flow calculation; otherwise, wind statistics were horizontally homogeneous and represented by Monin–Obukhov profiles. Numbers in parentheses are the standard error, expressed as a percentage.

		$(SC/Q)^{\text{obs}}$		$(SC/Q)^*$	Q^{LS}/Q
A	MO	f	2.15×10^{-2} (5%)	1.28×10^{-2} (1%)	1.68
A	MO	b		1.35×10^{-2} (5%)	1.60
B	MO	f	2.54×10^{-2} (2%)	1.42×10^{-2} (1%)	1.79
B	MO	b		1.44×10^{-2} (6%)	1.76
D	MO	f	1.94×10^{-3} (8%)	2.16×10^{-3} (1%)	0.90
D	MO	b		2.17×10^{-3} (10%)	0.90
A	3D	f	2.15×10^{-2} (5%)	2.70×10^{-2} (1%)	0.80
A	3D	b		2.57×10^{-2} (2%)	0.84
B	3D	f	2.54×10^{-2} (2%)	1.52×10^{-2} (1%)	1.67
B	3D	b		1.53×10^{-2} (2%)	1.66
D	3D	f	1.94×10^{-3} (8%)	1.87×10^{-3} (1%)	1.04
D	3D	b		1.95×10^{-3} (8%)	1.00

both treatments—and because forward detectors (i.e., the laser paths) must be attributed to a finite volume, it is required that in backward simulations they be treated as finite volume sources. Forward simulations were performed for configurations A, B, D (for which laser detectors were parallel to one or another of the sides of the plot). Particles were assigned a random starting position within the horizontal confines of the (physical) source (i.e., uniform release on $-3 \leq x, y \leq 3$ m) and initial height $z = z_0$ (forward source a parallelepiped with zero depth). Each laser detector was represented (whether as a forward detector or a backward source) as being a rectangular parallelepiped, aligned with the x or the y axis as need be, and defined by its centerpoint and its halfspans about that point on each axis. The longitudinal half-span was half the laser pathlength, while transverse halfspans were set to 0.2 m (note: the larger the detector volume is, the smaller is the statistical uncertainty; the 0.2 m halfspan was a compromise).

Table A1 demonstrates an excellent consistency of forward and backward simulations, and (secondarily, cf. Table 2) that assigning the laser paths a finite cross section as large as ± 0.2 m results in an alteration of the Q^{bLS}/Q ratio when the detector is very near the source. Although the forward–backward consistency is only what is expected in principle, some discussion is warranted. At the outset, all sources and all detectors had been consistently and identically treated as having a finite volume, characterized by three finite halfspans about a centerpoint—and (crucially) the physical source too had been represented by a slab of depth 0.3 m centered on $z = 0.2$ m, that same volume also serving as a residence time detector for backward simulations. However, in

that configuration, no matter how small the time step was, forward and backward simulations simply were not consistent. The forward-backward consistency reported by Table A1 was procured only after the realization that a rigorously systematic treatment of the forward source and the backward detector is needed. Thus, as stated earlier, all simulations for which results are shown in this paper treated the physical source as a plane on ground, and (in the backward treatment) estimated the concentration over the physical source by the touchdown method [Eq. (7)]. In summary, fLS and bLS provided consistent C/Q , provided that the time step was sufficiently small and that prescription of sources and detectors was consistent across both treatments.

REFERENCES

- Bourdin, P., and J. D. Wilson, 2008: Windbreak aerodynamics: Is CFD reliable? *Bound.-Layer Meteor.*, **126**, 181–208.
- Cai, X., G. Peng, X. Guo, and M. Y. Leclerc, 2008: Evaluation of backward and forward Lagrangian footprint models in the surface layer. *Theor. Appl. Climatol.*, **93**, 207–223.
- Flesch, T. K., J. D. Wilson, and E. Yee, 1995: Backward-time Lagrangian stochastic dispersion models, and their application to estimate gaseous emissions. *J. Appl. Meteor.*, **34**, 1320–1332.
- , —, L. A. Harper, B. P. Crenna, and R. R. Sharpe, 2004: Deducing ground-to-air emissions from observed trace gas concentrations: A field trial. *J. Appl. Meteor.*, **43**, 487–502.
- , —, —, and —, 2005a: Estimating gas emission from a farm using an inverse-dispersion technique. *Atmos. Environ.*, **39**, 4863–4874.
- , —, and —, 2005b: Deducing ground-to-air emissions from observed trace gas concentrations: A field trial with wind disturbance. *J. Appl. Meteor.*, **44**, 475–484.
- , —, —, R. Todd, and N. Cole, 2007: Determining ammonia emissions from a cattle feedlot with an inverse dispersion technique. *Agric. For. Meteorol.*, **144**, 139–155.
- , L. A. Harper, J. M. Powell, and J. D. Wilson, 2009: Inverse-dispersion calculation of ammonia emissions from Wisconsin dairy farms. *Trans. ASABE*, **52**, 253–265.
- Hanna, S. R., J. C. Chang, and D. G. Strimaitis, 1990: Uncertainties in source emission rate estimates using dispersion models. *Atmos. Environ.*, **24A**, 2971–2980.
- Laubach, J., F. M. Kelliher, T. W. Knight, H. Clark, G. Molano, and A. Cavanagh, 2008: Methane emissions from beef cattle—A comparison of paddock and animal-scale measurements. *Aust. J. Exp. Agric.*, **48**, 132–137.
- Leschziner, M. A., 2000: Turbulence modelling for separated flows with anisotropy-resolving closures. *Philos. Trans. Roy. Soc. London*, **358A**, 3247–3277.
- Loh, Z., R. Leuning, S. Zegelin, D. Etheridge, M. Bai, T. Naylor, and D. Griffith, 2009: Testing Lagrangian atmospheric dispersion modelling to monitor CO₂ and CH₄ leakage from geo-sequestration. *Atmos. Environ.*, **43**, 2602–2611.
- McGinn, S. M., K. A. Beauchemin, T. K. Flesch, and T. Coates, 2009: Performance of a dispersion model to estimate methane loss from cattle in pens. *J. Environ. Qual.*, **38**, 1796–1802.
- Plate, E. J., 1971: The aerodynamics of shelter belts. *Agric. Meteorol.*, **8**, 203–222.
- Pope, S. B., 2000: *Turbulent Flows*. Cambridge University Press, 771 pp.
- Raine, J. K., and D. C. Stevenson, 1977: Wind protection by model fences in a simulated atmospheric boundary layer. *J. Wind Eng. Ind. Aerodyn.*, **2**, 159–180.
- Richards, P. J., 1986: Wind protection in the vicinity of right angle wind break corners. *Proc. Ninth Australasian Fluid Mechanics Conference*, Auckland, New Zealand, 193–195.
- Santiago, J., F. Martin, A. Cuerva, N. Bezdenejnykh, and A. Sanz-Andrés, 2007: Experimental and numerical study of wind flow behind windbreaks. *Atmos. Environ.*, **41**, 6406–6420.
- Thomson, D. J., 1987: Criteria for the selection of stochastic models of particle trajectories in turbulent flows. *J. Fluid Mech.*, **180**, 529–556.
- Wilson, J. D., 1997: A field study of the mean pressure about a windbreak. *Bound.-Layer Meteor.*, **85**, 327–358.
- , 2004: Oblique, stratified winds about a shelter fence. Part II: Comparison of measurements with numerical models. *J. Appl. Meteor.*, **43**, 1392–1409.
- , 2007: Turbulent velocity distributions and implied trajectory models. *Bound.-Layer Meteor.*, **125**, 39–47.
- , 2008: Monin-Obukhov functions for standard deviations of velocity. *Bound.-Layer Meteor.*, **129**, 353–369.
- , and T. K. Flesch, 1993: Flow boundaries in random flight dispersion models: Enforcing the well-mixed condition. *J. Appl. Meteor.*, **32**, 1695–1707.
- , and —, 2003: Wind measurements in a square plot enclosed by a shelter fence. *Bound.-Layer Meteor.*, **109**, 191–224.
- , E. Yee, N. Ek, and R. d'Amours, 2009: Lagrangian simulation of wind transport in the urban environment. *Quart. J. Roy. Meteor. Soc.*, **135**, 1586–1602.
- Yee, E., and J. D. Wilson, 2007: On the presence of instability in Lagrangian stochastic trajectory models, and a method for its cure. *Bound.-Layer Meteor.*, **122**, 243–261.